Analysis and Optimization of Carrier Phase Displacement Angles for Modular Multilevel Converters With PSC–PWM

Bin Zhang, *Student Member, IEEE*, Jiapeng Yin, Qifan Yang, and Ningyi Dai, *Senior Member, IEEE*

***Abstract*—In the conventional implementations of phase-shifted carrier pulsewidth modulation (PSC–PWM) for modular multilevel converters (MMCs), different phases normally adopt identical carrier arrangements, neglecting the phase-to-phase carrier phase displacement (P2PCPD). This article presents a comprehensive analysis of the P2PCPD angles, focusing on their effects on the harmonic characteristics of the line-to-line voltages (LLVs) and common mode voltage (CMV). The selection criteria of the P2PCPD angles are proposed for different conditions in terms of the modulation index and the number of submodules (SMs) per arm of the MMC. It is revealed that the LLV and CMV harmonics cannot be minimized simultaneously, while a trade-off can be achieved between these two control objectives: a proper set of P2PCPD angles can be obtained which minimizes the CMV/LLV harmonic distortion meanwhile keeping the LLV/CMV harmonic distortion below a preset threshold. Simulations and experiments are conducted, and their results validate the theoretical findings.**

***Index Terms*—Common mode voltage (CMV), line-to-line voltage (LLV), modular multilevel converter (MMC), phase-shifted carrier pulsewidth modulation (PSC–PWM).**

I. INTRODUCTION

OVER the last two decades, the modular multilevel converter (MMC) topology has been extensively studied and utilized in various high/medium voltage (MV) applications due to its numerous advantages, such as modularity, high reliability, and high-quality output waveforms [1], [2], [3], [4], [5], [6]. In order to fully exploit these benefits, various control and modulation methods have been proposed and investigated for MMC systems.

According to the switching frequency features, the modulation methods for MMC can be classified into two types, the low and high switching frequency methods. Between them, the low switching frequency modulation methods, such as nearest level modulation method [7], [8], [9], are usually applied to high voltage applications, which require a significant number of cascaded submodules (SMs). In contrast, the high switching frequency modulation methods, such as phase disposition sinusoidal pulsewidth modulation (PD–SPWM) method [10], [11], [12], [13], [14] and phase shifted carrier pulsewidth modulation (PSC–PWM) method [18], [19], [20], [21], [22], [23], [24], [25], are suitable for MV applications with smaller requirements in the cascaded SMs number.

However, the PD–SPWM method worsens the energy balance among SMs and cannot be implemented using a distributed approach [15], [16]. Due to these existing drawbacks in the PD–SPWM method, PSC–PWM method is more preferred in MMC-based MV applications. The PSC–PWM method was first proposed for the full-bridge cascaded converter (FBCC) [17]. With properly allocated carriers for different SMs, the equivalent switching frequencies can be increased to N times the switching frequencies, where N is the total number of the cascaded SMs. Therefore, the output voltage harmonics can be significantly reduced. Different from the FBCC, two groups of carriers exist in each phase of MMC, one for the upper arm and the other for the lower arm [18]. Li et al. [19] introduced a phase displacement angle between the two group carriers in the upper and lower arms, which can further enhance the harmonic characteristics of the half-bridge (HB) or full-bridge (FB) based MMC systems. Based on [19], Lu et al. [20] improved the PSC–PWM method to evenly distribute the switching losses between the HBSMs and the FBSMs in the hybrid MMC topology.

Recently, the PSC–PWM techniques were further investigated under various MMC topology, control strategies, and application scenarios [21], [22], [23], [24]. Xu et al. [21] extended the PSC–PWM scheme to the hybrid MMC with boosted modulation index. Jiang et al. [22] improved the PSC–PWM scheme for the HB-MMC system under the SM capacitor voltage reduction control strategy. Thakur et al. [23] comprehensively optimized the PSC–PWM scheme for the FB-MMC with the boosted working mode. Li et al. [24] proposed a decoupled PSC–PWM-based modulation scheme to eliminate the low-frequency harmonics under the circulating current suppressing control strategy.

Manuscript received 20 July 2023; revised 6 November 2023 and 17 January 2024; accepted 24 February 2024. Date of publication 4 March 2024; date of current version 19 April 2024. This work was supported in part by the Macau Science and Technology Development Fund under Grant 0029/2022/AMJ and Grant 001/2024/SKL, in part by the National Key Research and Development Program of China under Grant 2022YFE0205100, and in part by the University of Macau under Grant MYRG2022-00104-FST. Recommended for publication by Associate Editor G. Konstantinou. *(Corresponding author: Jiapeng Yin.)*

The authors are with the State Key Laboratory of Internet of Things for Smart City and Department of Electrical and Computer Engineering, University of Macau, Macau 999078, China (e-mail: yc17429@umac.mo; jpyin1992@gmail.com; yc07464@umac.mo; nydai@um.edu.mo).

Color versions of one or more figures in this article are available at https://doi.org/10.1109/TPEL.2024.3372611.

Digital Object Identifier 10.1109/TPEL.2024.3372611

Although the carrier arrangements in each single phase have been extensively investigated in the literature, the carrier phase displacements among different phases have not been properly studied. Recently, Zhou et al. [25] introduced the nonzero phase-to-phase carrier phase displacement (P2PCPD) angles in MMC systems, mainly for improving the harmonic performance of the line-to-line voltages (LLVs) in the traditional $(N+1)$ level PSC-PWM scheme. Zhou et al. [25] neglected the effects of the modulation index on the P2PCPD angles, and the analysis is limited to the LLV harmonics, neglecting other relevant control objectives of the MMC such as the common mode voltage (CMV). To bridge these research gaps, this article conducts a comprehensive analysis of the P2PCPD angles for an MMC with PSC–PWM, with the main contributions summarized as follows.

1) The effects of P2PCPD angles on the harmonic characteristics of the LLVs and also the CMV are analyzed.
2) Selection criteria of P2PCPD angles are proposed for different conditions in terms of the modulation index and the number of SMs per arm of the MMC.
3) The relations between the harmonic minimization of the LLVs and CMV are revealed. A flexible trade-off can be achieved between both control objectives. Proper P2PCPD angles can be derived, which minimize the CMV harmonic contents while keeping the LLV harmonic distortion below a preset threshold, and vice versa.

This rest of this article is organized as follows. Section II briefly reviews the basic mathematical models and the PSC-PWM scheme for MMC. Section III analyzes the harmonic suppressing properties of the LLVs and CMV in detail. Section IV presents the P2PCPD angle design method to achieve a flexible trade-off between LLV and CMV harmonic suppressions. Simulation and experimental results are given in Sections V and VI, respectively. Finally, Section VII concludes this article.

II. REVIEW OF THE MMC TOPOLOGY AND THE PSC–PWM MODULATION SCHEME

A. Mathematical Modeling of the MMC Topology

Fig. 1 shows the typical structure of a three-phase MMC, which comprises three parallel phase legs. Each phase leg contains an upper arm and a lower arm, and each arm is formed with N cascade-connected HBSMs and an arm inductor L_{arm}. The main variables and reference directions are all depicted in Fig. 1, where variable j ($j \in \{a, b, c\}$) uniformly denotes three phases A, B, and C; variable x ($x \in \{u, l\}$) uniformly denotes the upper arm and the lower arm; variable k ($k \in \{1, 2, 3, \ldots, N\}$) uniformly denotes the SM's position in an arm. In addition, the O point is the midpoint of the dc-link, and N' is the neutral point of the ac system.

The simplified equivalent circuits of the MMC are shown in Fig. 2(a), which can be decoupled into two parts, namely the ac part and the dc part [8], as shown in Fig. 2(b) and (c), respectively. The ac part shows the interaction characteristics between the MMC and the ac system, while the dc part shows the interaction characteristics between the MMC and the dc link.

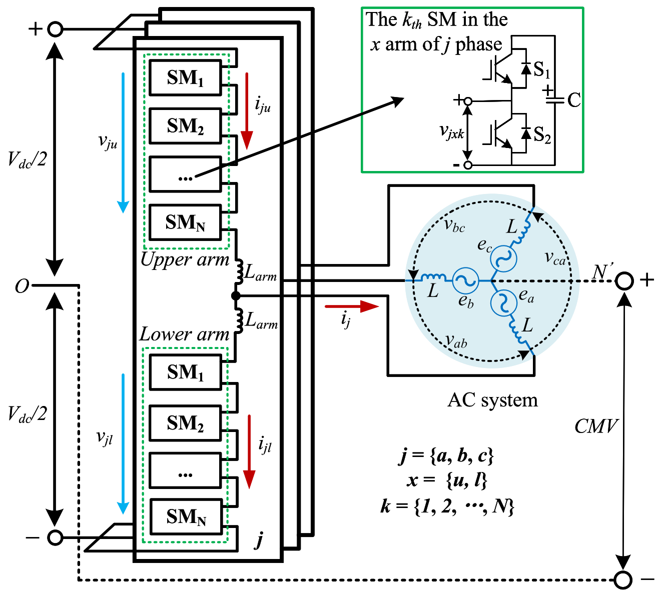

Fig. 1. Topology of a three-phase MMC.

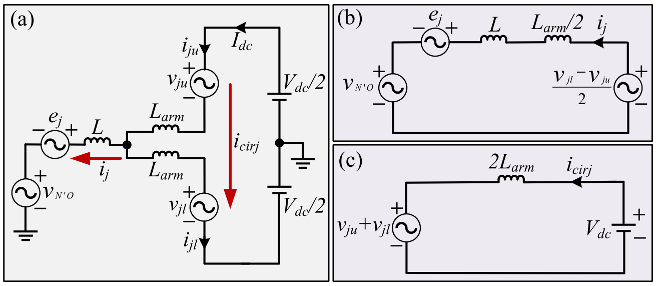

Fig. 2. Equivalent circuits of the MMC. (a) Single-phase equivalent circuit. (b) AC part equivalent circuit. (c) DC part equivalent circuit.

The mathematical model of the ac part can be expressed as

$$\begin{cases} v_{jo} = L\frac{di_j}{dt} + e_j + v_{N'O} = \frac{v_{jl}-v_{ju}}{2} - \frac{L_{\text{arm}}}{2}\frac{di_j}{dt} \\ i_j = i_{ju} - i_{jl} \end{cases} \tag{1}$$

where v_{jo} is the ac-terminal voltage of the MMC; L is the coupling inductor between the MMC and the ac system; i_j is the ac output current; e_j denotes the ac system voltage; $v_{N'O}$ is the CMV, which represents the voltage difference between N' and O point; v_{ju} and v_{jl} are the voltages of the upper and lower arms, respectively; i_{ju} and i_{jl} are the currents of the upper and lower arms, respectively.

On the other hand, the mathematical model of the dc part can be expressed as

$$\begin{cases} L_{\text{arm}}\frac{di_{\text{cirj}}}{dt} = \frac{V_{\text{dc}}}{2} - \frac{v_{jl}+v_{ju}}{2} \\ i_{\text{cirj}} = \frac{i_{jl}+i_{ju}}{2} \end{cases} \tag{2}$$

where V_{dc} is the actual voltage of the dc-link; i_{cirj} is the circulating current flowing along the phase j leg and the dc side and can be controlled by the sum of the upper and lower arm voltages.

Based on (1) and adding the three-phase equations, the CMV of the MMC can be finally represented as

$$\begin{aligned} v_{\text{cmv}} &= \frac{1}{6}[(v_{al}+v_{bl}+v_{cl})-(v_{au}+v_{bu}+v_{cu})] \\ &= \frac{1}{3}(v_{ao}+v_{bo}+v_{co}). \end{aligned} \tag{3}$$

B. Modulation Signals

Suppose the ac-terminal voltage of MMC is represented as

$$v_{jo} = V_m \cos(\omega_0 t + \varphi_j) \tag{4}$$

where ω_0 is the fundamental angular frequency; V_m is the magnitude of the ac-terminal voltage v_{jo}; φ_j is the initial phase angle of the ac-terminal voltage ($\varphi_j = 0, -2\pi/3, 2\pi/3$).

Based on (1) and (2), and neglecting the voltage drop across the arm inductors, the lower and upper arm voltages can be expressed as

$$\begin{cases} v_{jl} = \frac{V_{\text{dc}}}{2} + V_m \cos(\omega_0 t + \varphi_j) \\ v_{ju} = \frac{V_{\text{dc}}}{2} - V_m \cos(\omega_0 t + \varphi_j). \end{cases} \tag{5}$$

Assuming the SMs of each arm are operated in balance with each other, then the arm voltage (5) should be equally divided across the SMs. Hence, the output voltage of each SM in the upper/lower arm can be expressed as

$$\begin{cases} v_{jlk} = \frac{1}{N}\left[\frac{V_{\text{dc}}}{2} + V_m \cos(\omega_0 t + \varphi_j)\right] \\ v_{juk} = \frac{1}{N}\left[\frac{V_{\text{dc}}}{2} - V_m \cos(\omega_0 t + \varphi_j)\right] \end{cases} \tag{6}$$

For simplicity, the SM capacitor voltage ripple is neglected, and the SM capacitor voltages are all assumed to equal V_{dc}/N [23]. Normalizing (6) by V_{dc}/N, the modulation signals for each SM in the upper/lower arm can be expressed as

$$\begin{cases} m_{jlk} = \frac{1}{2} + \frac{M}{2}\cos(\omega_0 t + \varphi_j) \\ m_{juk} = \frac{1}{2} - \frac{M}{2}\cos(\omega_0 t + \varphi_j) \end{cases} \tag{7}$$

where M is the modulation index and equals to $2V_m/V_{\text{dc}}$.

C. PSC–PWM Scheme of the MMC System

Fig. 3 shows the PSC–PWM scheme of the MMC system. For the k_{th} SM in the x arm of phase j, the triangular carrier signal C_{jxk} and the modulation signal m_{jxk} are compared when implementing the PCS–PWM scheme. Hence, in each arm, there are N carrier signals in the PSC–PWM scheme. To get the best harmonic performance at each arm, the N carriers in each arm are sequentially phase-shifted by $2\pi/N$ angle. Then, to further allocate the carriers in each phase, the N carriers of the upper arm are phase shifted by θ angle from the N carriers in the lower arm [17]. In this article, θ is referred as to the arm-to-arm carrier phase displacement (A2ACPD) angle.

Apart from the angle θ, the P2PCPD angles (δ_1 and δ_2) are also considered in this article. As shown in Fig. 3, δ_1 is the phase displacement angle between the phase b carriers and the phase a carriers, while δ_2 is the phase displacement angle between the phase c carriers and the phase a carriers. For the convenience of later analysis, we assume the initial angle of the carrier signal of the first SM in the lower arm is δ_j. Then, δ_1 can be expressed as $(\delta_b - \delta_a)$, while δ_2 can be expressed as $(\delta_c - \delta_a)$. Due to the symmetry of three-phase systems, δ_1 and δ_2 are constrained between 0 and $2\pi/N$.

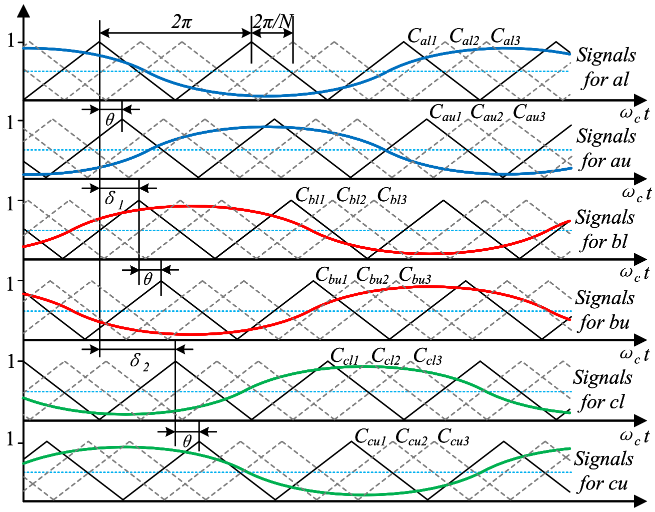

Fig. 3. PSC–PWM scheme for three-phase MMC.

III. ANALYSIS AND DESIGN OF THE P2PCPD ANGLES IN MMC SYSTEMS

The Double Fourier method [26] can effectively calculate the harmonic components of the waveforms controlled by double independently periodic variables, such as the output voltage waveform of a PWM switched converter. In this section, the Double-Fourier method [26] is employed to analyze the effects of the P2PCPD angles on the LLV and CMV harmonic performances for the MMC systems. Based on these theoretical analysis, two optimal working mode are developed, and the corresponding selection criteria are proposed for various operating conditions.

A. Double-Fourier Analysis of the Phase Voltage and the Circulating Current

Based on (1) and (7), and neglecting the voltage drop across the arm inductors, the phase voltage v_{jo} can be finally expressed as [25]

$$\begin{aligned} v_{jo} = {} & \frac{MV_{\text{dc}}}{2}\cos(\omega_0 t + \varphi_j) + \sum_{m=1}^{\infty}\sum_{n=-\infty}^{\infty} K_{mn} \\ & \times \cos\left[Nm(\omega_c t + \delta_j) + n(\omega_0 t + \varphi_j) + \frac{Nm(\theta - \pi)}{2}\right] \end{aligned} \tag{8}$$

$$\begin{aligned} K_{mn} = {} & \frac{2V_{\text{dc}}}{m\pi N} \times J_n\left(\frac{MNm\pi}{2}\right) \times \sin\left[\frac{(Nm+n)\pi}{2}\right] \\ & \times \cos\left[\frac{Nm(\theta-\pi)}{2}\right] \end{aligned} \tag{9}$$

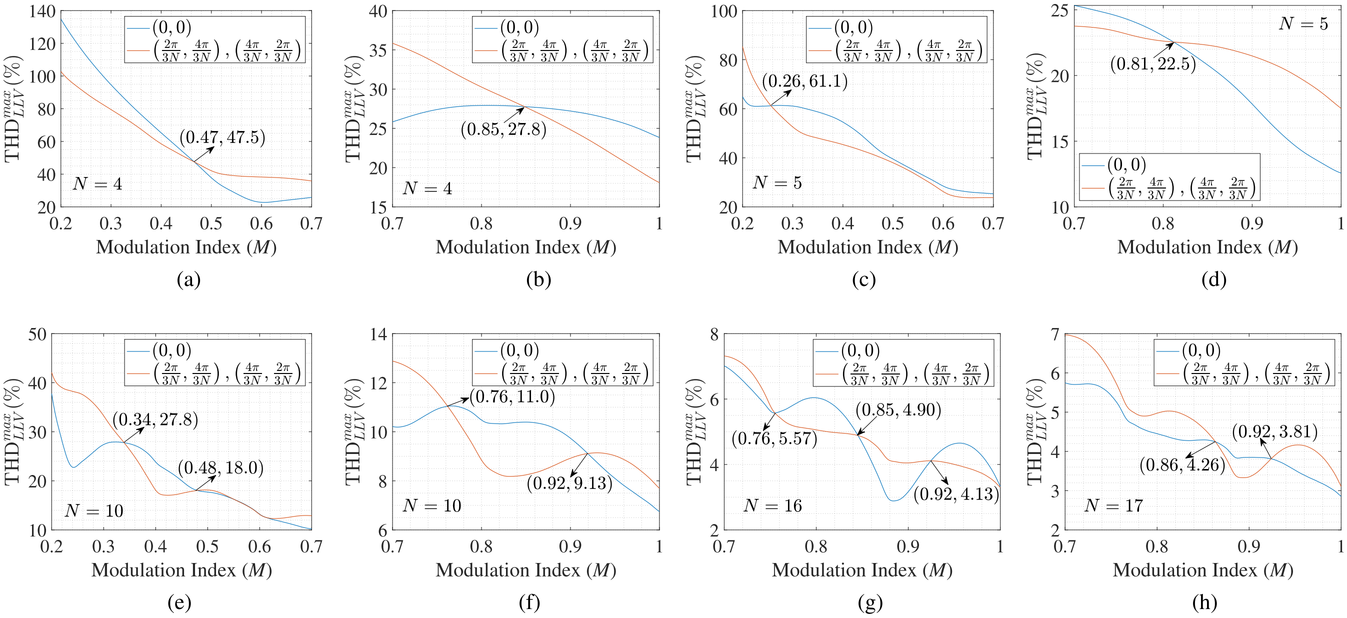

(a) (b) (c) (d)

(e) (f) (g) (h)

Fig. 4. Comparisons of the $\mathrm{THD}_{\mathrm{LLV}}^{\max}$ values under different N, M, and (δ_1, δ_2). (a) $N = 4, 0.2 \leq M \leq 0.7, \theta = 0$. (b) $N = 4, 0.7 \leq M \leq 1, \theta = 0$. (c) $N = 5, 0.2 \leq M \leq 0.7, \theta = \frac{\pi}{N}$. (d) $N = 5, 0.7 \leq M \leq 1, \theta = \frac{\pi}{N}$. (e) $N = 10, 0.2 \leq M \leq 0.7, \theta = 0$. (f) $N = 10, 0.7 \leq M \leq 1, \theta = 0$. (g) $N = 16, 0.7 \leq M \leq 1, \theta = 0$. (h) $N = 17, 0.7 \leq M \leq 1, \theta = \frac{\pi}{N}$.

where ω_c is the carrier angular frequency; $J_n(x)$ is the Bessel function of the first kind, with order n and argument x; K_{mn} is the magnitude of each side-band harmonic of the phase voltage v_{jo}. Furthermore, $\{m, n\}$ defines the n_{th} side-band harmonic within the m_{th} carrier harmonic group.

On the other hand, based on (2) and (7), the harmonic expression of the circulating current can be expressed as [25]

$$i_{ciarj} = \frac{I_{\text{dc}}}{3} - \sum_{m=1}^{\infty}\sum_{n=-\infty}^{\infty}\frac{V_{\text{dc}} \times \sin\left[\frac{(Nm+n)\pi}{2}\right]}{m\pi N L_{\text{arm}}(m\omega_0 + n\omega_c)} \times J_n\left(\frac{MNm\pi}{2}\right) \times \sin\left[\frac{Nm(\theta-\pi)}{2}\right] \times \cos\left[Nm\left(\omega_c t + \delta_j + \frac{\theta-\pi}{2}\right) + n(\omega_0 t + \varphi_j)\right] \tag{10}$$

where I_{dc} denotes the total dc-link current. And due to the symmetry among the three phase legs, the circulating current of each phase leg contains a dc component which equals $I_{\text{dc}}/3$. More derivation details about (8) and (10) can be found in [25].

It is clear from (8) and (10) that the P2PCPD angles only influence the initial phase angle of the phase voltage harmonics and the circulating current harmonics. Consequently, the conclusions regarding the A2ACPD angle in [19] remain valid even when considering the P2PCPD angle. For the $(N + 1)$ level PSC–PWM scheme, the A2ACPD angle θ should still be set to 0 (or π/N) for N is even (or odd).

B. Double-Fourier Analysis of the LLVs

According to (8), the LLVs can be deduced as

$$\begin{cases} v_{ab} = \frac{\sqrt{3}}{2}MV_{\text{dc}}\cos\left(\omega_0 t + \frac{\pi}{6}\right) \\ \quad + \sum_{m=1}^{\infty}\sum_{n=-\infty}^{\infty} R_{mn}^{ab} \times \cos\left[Nm\omega_c t + n\omega_0 t + \frac{Nm\delta_1}{2} + \frac{3Nm\theta - Nm\pi}{6} - \frac{(2n+1)\pi}{3}\right] \\ v_{\text{bc}} = \frac{\sqrt{3}}{2}MV_{\text{dc}}\sin(\omega_0 t) \\ \quad + \sum_{m=1}^{\infty}\sum_{n=-\infty}^{\infty} R_{mn}^{\text{bc}} \times \cos\left[Nm\omega_c t + n\omega_0 t + \frac{Nm(\delta_1+\delta_2)}{2} + \frac{Nm(\theta-\pi)}{2}\right] \\ v_{ca} = \frac{\sqrt{3}}{2}MV_{dc}\cos\left(\omega_0 t + \frac{5\pi}{6}\right) \\ \quad + \sum_{m=1}^{\infty}\sum_{n=-\infty}^{\infty} R_{mn}^{ca} \times \cos\left[Nm\omega_c t + n\omega_0 t + \frac{Nm\delta_2}{2} + \frac{3Nm\theta - 5Nm\pi}{6} + \frac{(2n+1)\pi}{3}\right] \end{cases} \tag{11}$$

where R_{mn}^{y} is the magnitude of each side-band harmonic of the line-to-line voltage v_y $(y = ab, bc, ca)$ and can be expressed as

$$\begin{cases} R_{mn}^{ab} = 2K_{mn}\sin\left(\frac{Nm\delta_1}{2} - \frac{n\pi}{3}\right) \\ R_{mn}^{bc} = 2K_{mn}\sin\left[\frac{Nm(\delta_2-\delta_1)}{2} + \frac{2n\pi}{3}\right] \\ R_{mn}^{ca} = 2K_{mn}\sin\left(-\frac{Nm\delta_2}{2} - \frac{n\pi}{3}\right) \end{cases}. \tag{12}$$

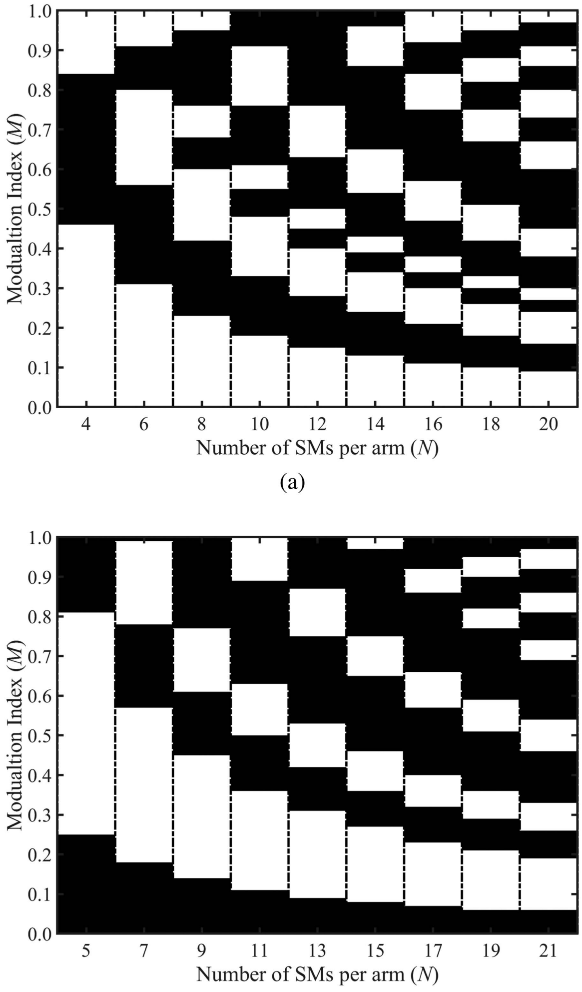

(a)

(b)

Fig. 5. Optimal P2PCPD angle selection criteria for the Min-LVH (Min-CMVH) mode under different M and N. (a) N is Even, $\theta = 0$. (b) N is odd, $\theta = \pi/N$.

From (11) and (12), it is clear that the harmonic magnitude components of the LLVs strongly depend on the P2PCPD angles and the converter operating conditions, which are mainly determined by the modulation index (M) and the number of SMs (N). To better study the effects of P2PCPD angles on the harmonic performance of the LLVs, different carrier harmonic groups need to be included. Here, only the first three carrier harmonic groups ($m = 1, 2, 3$) are considered due to their relatively large proportion among all the harmonics of LLVs.

Defining the maximum total harmonic distortion (THD) of the three-phase LLVs as

$$\mathrm{THD}_{LLV}^{\max} = \max\{\mathrm{THD}_{ab}, \mathrm{THD}_{bc}, \mathrm{THD}_{ca}\} \tag{13}$$

$$\mathrm{THD}_{y} = \frac{2}{\sqrt{3}MV_{\mathrm{dc}}}\sqrt{\sum_{m=1}^{3}\sum_{n=-\infty}^{\infty} {R_{mn}^{y}}^{2}} \tag{14}$$

where THD_y is the THD of the LLV v_y. In this article, the working mode with the minimum $\mathrm{THD}_{\mathrm{LLV}}^{\max}$ value is referred to as the minimum LLV harmonics (Min-LVH) mode.

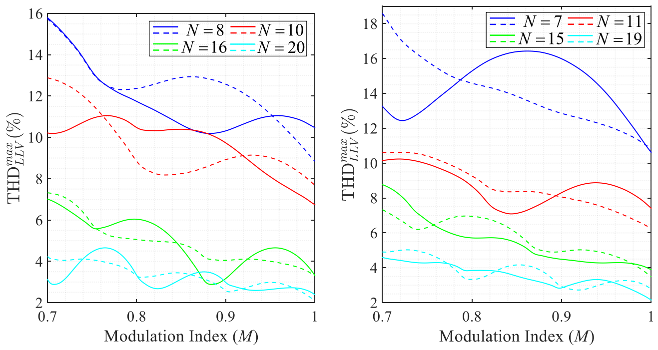

(a)

(b)

Fig. 6. Comparisons of $\mathrm{THD}_{\mathrm{LLV}}^{\max}$ values when using different P2PCPD angles across various values of N. (a) N is even, $0.7 \leq M \leq 1, \theta = 0$. (b) N is odd, $0.7 \leq M \leq 1, \theta = \pi/N$.

TABLE I
CIRCUIT PARAMETERS FOR CASE 1 AND EXPERIMENT

Symbol	Quantity	Value
V_{dc}	DC-link voltage	200 V
N	Number of SMs per arm	4
C	SM capacitance	0.41 mF
L_{arm}	Self/mutual inductance of buffer inductor	2 mH
f_c	SM switching frequency	1000 Hz
f_0	Fundamental frequency	50 Hz
R_{load}	Load resistance	100 Ω
PF	Power factor for load	1.00

By exhaustively evaluating the $\mathrm{THD}_{\mathrm{LLV}}^{\max}$ values for all P2PCPD angle pairs under different N and M, it is found that:

1) The P2PCPD angle corresponding to the minimum value of $\mathrm{THD}_{\mathrm{LLV}}^{\max}$ is not always (0, 0), but may also be $(\frac{2\pi}{3N}, \frac{4\pi}{3N})$ or $(\frac{4\pi}{3N}, \frac{2\pi}{3N})$ in some operating conditions. These operating conditions are determined by both M and N.
2) The P2PCPD angle pairs $(\frac{2\pi}{3N}, \frac{4\pi}{3N})$ and $(\frac{4\pi}{3N}, \frac{2\pi}{3N})$ share the same value of $\mathrm{THD}_{\mathrm{LLV}}^{\max}$.

To provide a quantitative representation of these findings, Fig. 4 compares the $\mathrm{THD}_{\mathrm{LLV}}^{\max}$ values under different cases. It becomes clear that the optimal P2PCPD angle pair under the Min-LVH mode varies with M and N. For instance, as shown in Fig. 4(a) and (b), the nonzero P2PCPD angle pairs $(\frac{2\pi}{3N}, \frac{4\pi}{3N})$ or $(\frac{4\pi}{3N}, \frac{2\pi}{3N})$ should be selected when $0.2 \leq M \leq 0.47$ and $0.85 \leq M \leq 1$; whereas the conventional zero P2PCPD angle pair (0, 0) should still be chosen when $0.47 < M < 0.85$. A further comparison of the eight subfigures in Fig. 4 clarifies that the selection criteria are also subject to N. Consequently, the P2PCPD angle pair must be flexibly selected according to the specific operating conditions. In addition, for the convenience of later analysis, the corresponding intersection points where the optimal angle varies are also marked in Fig. 4.

Fig. 5 further summarizes the selection criteria for P2PCPD angle pairs under the Min-LVH mode with a wider range of M and N. In Fig. 5, the x-axis and y-axis represent the number of SMs per arm (N) and the modulation index (M), respectively. The optimal P2PCPD angle pair can be determined based on the color of the region where the operating point (N, M) is located. When the MMC operates in the black regions of Fig. 5,

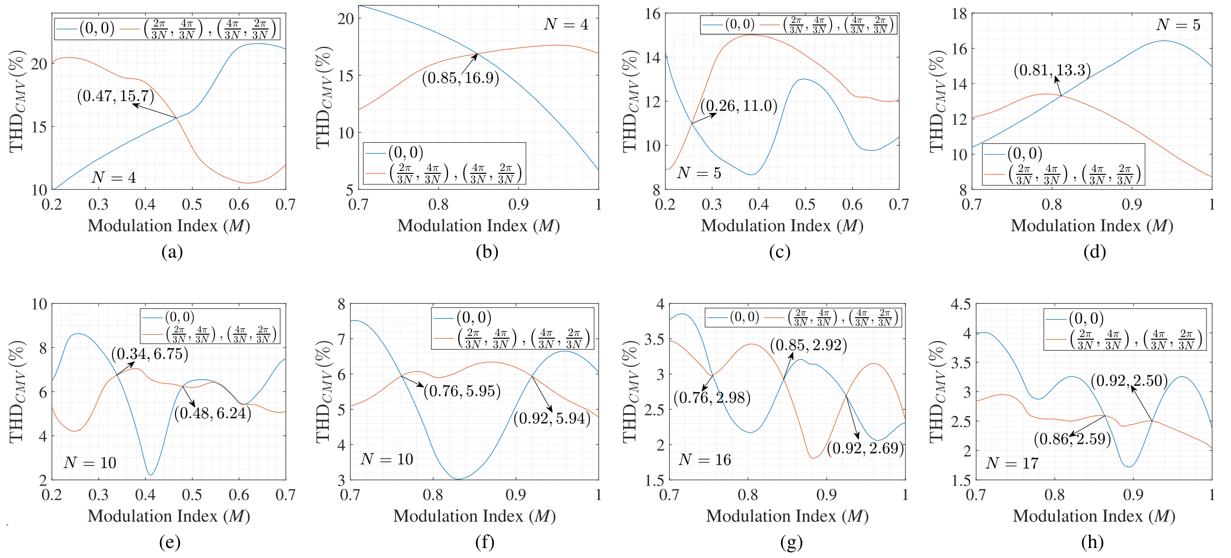

(a) (b) (c) (d)

(e) (f) (g) (h)

Fig. 7. Comparisons of the THD$_{\text{CMV}}$ values under different N, M, and (δ_1, δ_2). (a) $N = 4, 0.2 \leq M \leq 0.7, \theta = 0$. (b) $N = 4, 0.7 \leq M \leq 1, \theta = 0$. (c) $N = 5, 0.2 \leq M \leq 0.7, \theta = \frac{\pi}{N}$. (d) $N = 5, 0.7 \leq M \leq 1, \theta = \frac{\pi}{N}$. (e) $N = 10, 0.2 \leq M \leq 0.7, \theta = 0$. (f) $N = 10, 0.7 \leq M \leq 1, \theta = 0$. (g) $N = 16, 0.7 \leq M \leq 1, \theta = 0$. (h) $N = 17, 0.7 \leq M \leq 1, \theta = \frac{\pi}{N}$.

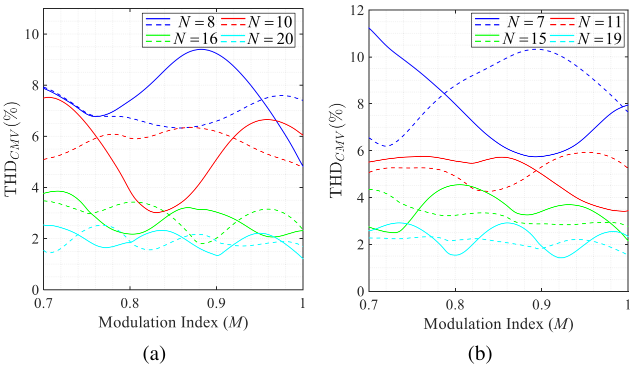

(a) (b)

Fig. 8. Comparisons of THD$_{\text{CMV}}$ values when using different P2PCPD angles across various values of N. (a) N is even, $0.7 \leq M \leq 1, \theta = 0$. (b) N is odd, $0.7 \leq M \leq 1, \theta = \pi/N$.

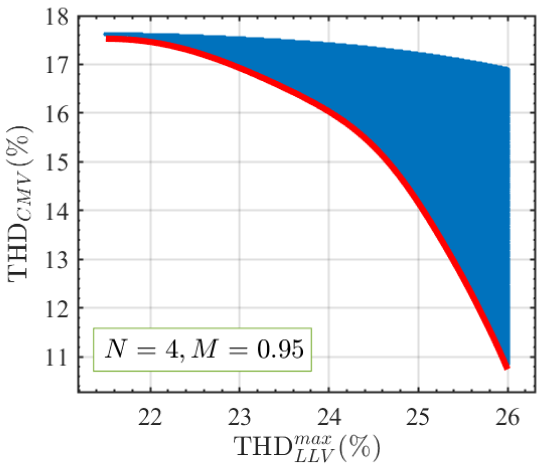

Fig. 9. Possible harmonic distortions of the LLVs and CMV under all P2PCPD angle pairs when $M = 0.95$ and $N = 4$.

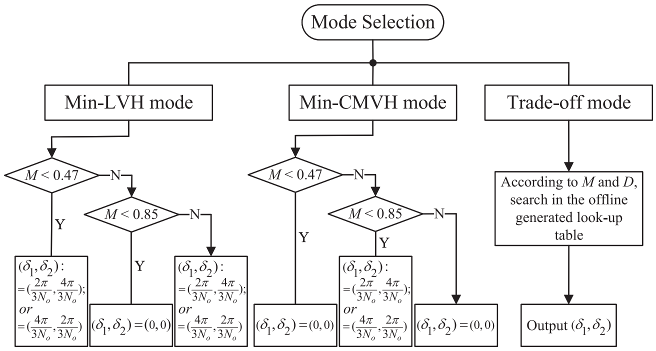

Fig. 10. Overall flowchart of the implementation of the proposed method for $N = N_o$ ($N_o = 4$ is taken as an example).

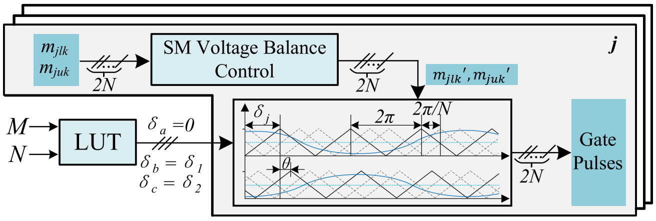

Fig. 11. Overall framework of the proposed PSC–PWM modulation for an MMC.

(0, 0) should be selected as the P2PCPD angle pair for the Min-LVH mode. Conversely, when the MMC operates in the white regions of Fig. 5, $(\frac{2\pi}{3N}, \frac{4\pi}{3N})$ or $(\frac{4\pi}{3N}, \frac{2\pi}{3N})$ should be selected as the P2PCPD angle pair for the Min-LVH mode. In addition, it can be seen that the alternations of black and white regions become more frequent for higher values of N. In other words, the optimal P2PCPD angle pair under the Min-LVH mode becomes more sensitive to changes in the modulation index M for higher N values.

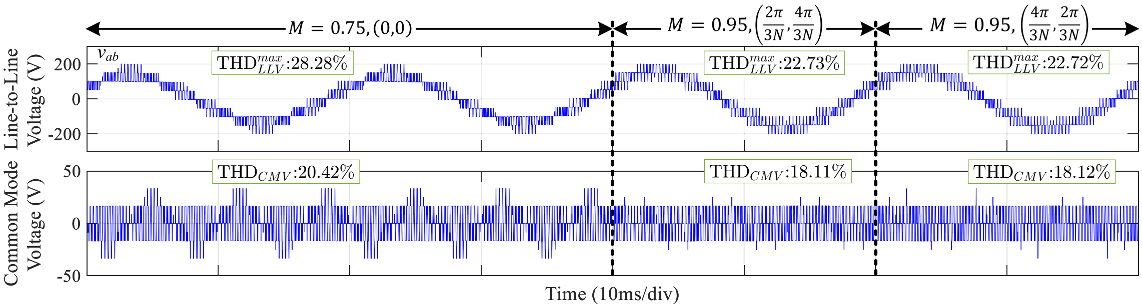

Fig. 12. Simulation waveforms of the Min-LVH mode at $N = 4$ across different modulation indexes.

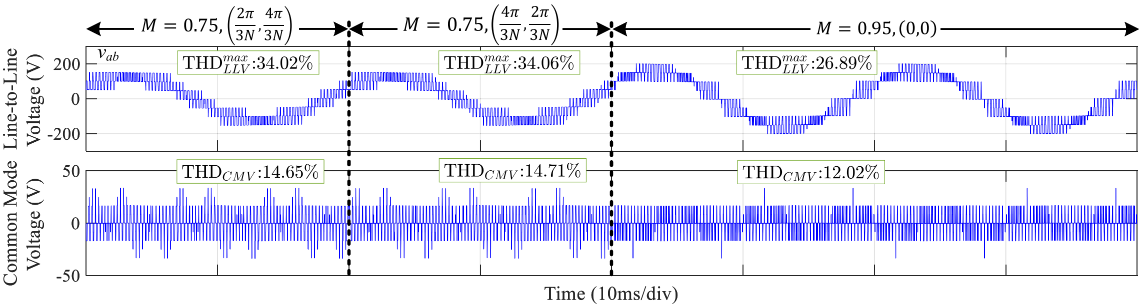

Fig. 13. Simulation waveforms of the Min-CMVH mode at $N = 4$ across different modulation indexes.

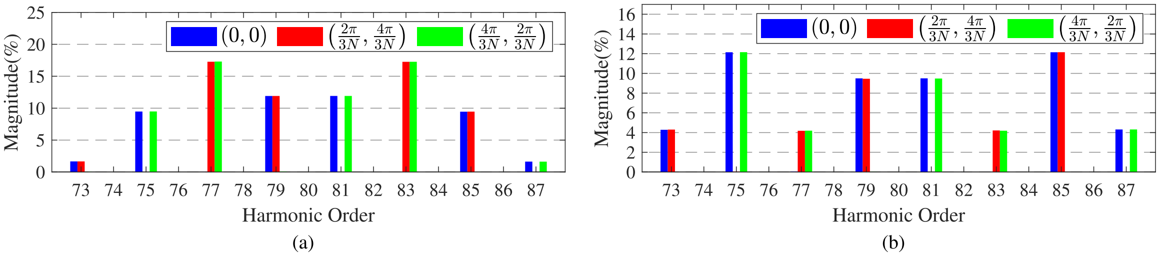

Fig. 14. Simulation harmonic spectrum of the first carrier harmonic group of the LLVs at $N = 4$ across different modulation indexes. (a) $M = 0.75$. (b) $M = 0.95$.

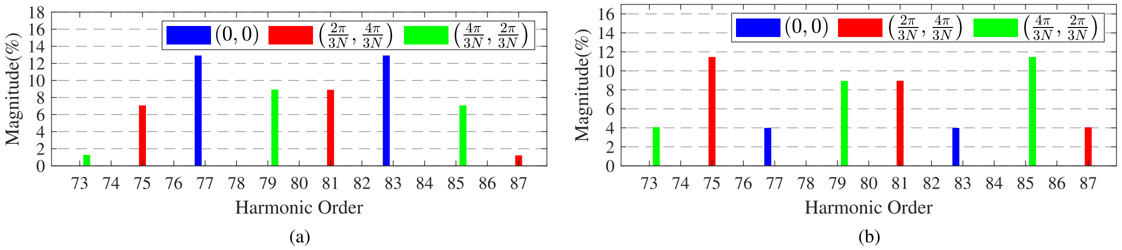

Fig. 15. Simulation harmonic spectrum of the first carrier harmonic group of the CMV at $N = 4$ across different modulation indexes. (a) $M = 0.75$. (b) $M = 0.95$.

TABLE II
SIMULATION THD PERFORMANCE AT $N = 4$ ACROSS DIFFERENT M AND (δ_1, δ_2)

Item	$M = 0.75$			$M = 0.95$			
	$(0,0)$	$\left(\frac{2\pi}{3N}, \frac{4\pi}{3N}\right)$	$\left(\frac{4\pi}{3N}, \frac{2\pi}{3N}\right)$	$(0,0)$	$\left(\frac{2\pi}{3N}, \frac{4\pi}{3N}\right)$	$\left(\frac{4\pi}{3N}, \frac{2\pi}{3N}\right)$	$(0.24, 0.48)$
$\mathrm{THD}_{\mathrm{LLV}}^{\max}$ (%)	28.28	34.02	34.06	26.89	22.73	22.72	25.99
$\mathrm{THD}_{\mathrm{CMV}}$ (%)	20.42	14.65	14.71	12.02	18.11	18.12	15.09

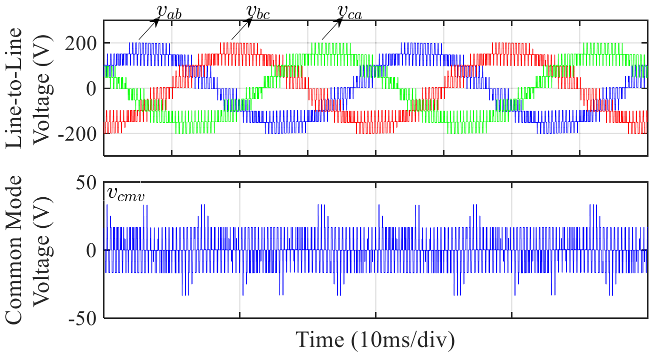

Fig. 16. Simulation waveforms of the LLVs and the CMV when $N = 4$, $M = 0.95$ and $(\delta_1, \delta_2) = (0.24, 0.48)$.

In Fig. 6, the differences in LLV harmonic performance when using different P2PCPD angle pairs are compared across various values of N. The solid line denotes the P2PCPD angle pair (0, 0), while the dotted line denotes the P2PCPD angle pair $(\frac{2\pi}{3N}, \frac{4\pi}{3N})$ or $(\frac{4\pi}{3N}, \frac{2\pi}{3N})$. As can be seen in Fig. 6, although the THD of LLVs generally decreases with the increase of N, the relative differences in using different P2PCPD angle pairs are still clear. This indicates that the proposed selection criteria for the Min-LVH mode remain effective when N is increased between 10 and 20. Therefore, the proposed selection criteria for Min-LVH mode are suitable for MV applications [27], [28]. For example, the MMC-based MV motor drive products are available in Siemens with 4–12 SMs per arm [28]. However, due to the inherent characteristics of the PSC-PWM scheme [4], [29], the proposed selection criteria are unsuitable for high-voltage applications with large numbers of SMs.

C. Double-Fourier Analysis of the CMV

CMV is another issue that needs to be concerned in the design of MMC systems. High CMV can cause several problems. For motor driving applications, CMV can cause induced shaft voltages, bearing currents, mechanical vibrations, and winding insulation damage [30], [31], [32], [33]. For photovoltaic (PV) systems, CMV often generates common mode currents, which may increase power losses, degrade the PV-arrays characteristics, accelerate aging, and increase the harmonic distortions of the output currents and voltages [34], [35], [36]. This section aims to analyze the effects of P2PCPD angle pairs on CMV theoretically.

Substituting (8) into (3), the CMV can be deduced as

$$v_{\mathrm{cmv}} = \sum_{m=1}^{\infty} \sum_{n=-\infty}^{\infty} Q_{mn} \times \cos\left(Nm\omega_c t + n\omega_0 t + \phi_{mn}\right) \tag{15}$$

$$Q_{mn} = \frac{K_{mn}}{3} \sqrt{\left\{\begin{array}{l} 3 + 2\cos\left(Nm\delta_1 - \frac{2n\pi}{3}\right) \\ +2\cos\left(Nm\delta_2 + \frac{2n\pi}{3}\right) \\ +2\cos\left[Nm\left(\delta_2 - \delta_1\right) + \frac{4n\pi}{3}\right] \end{array}\right\}} \tag{16}$$

TABLE III
CIRCUIT PARAMETERS FOR CASE 2

Symbol	Quantity	Value
V_{dc}	DC-link voltage	8000 V
N	Number of SMs per arm	10
C	SM capacitance	5 mF
L_{arm}	Self/mutual inductance of buffer inductor	4 mH
f_c	SM switching frequency	400 Hz
f_0	Fundamental frequency	50 Hz
$R_{\mathrm{load\,1}}$, $L_{\mathrm{load\,1}}$	Resistance and inductance of Load 1	$10\ \Omega, 10$ mH
PF$_1$	Power factor for Load 1	0.95
$R_{\mathrm{load\,2}}$, $L_{\mathrm{load\,2}}$	Resistance and inductance of Load 2	$2\ \Omega, 33$ mH
PF$_2$	Power factor for Load 2	0.19

$$\phi_{mn} = -\arctan \frac{\sum_{j=a,b,c} \sin\left[Nm\delta_j + n\varphi_j + \frac{Nm(\theta-\pi)}{2}\right]}{\sum_{j=a,b,c} \cos\left[Nm\delta_j + n\varphi_j + \frac{Nm(\theta-\pi)}{2}\right]} \tag{17}$$

where Q_{mn} is the magnitude of each side-band harmonic of v_{cmv}; ϕ_{mn} is the initial phase angle of each side-band harmonic of v_{cmv}.

From (15) and (16), it is clear that the CMV only includes the harmonics at integer multiples of the carrier frequency and their side-band harmonics. In addition, it is worth noting that the harmonic magnitudes of the CMV also depend on the P2PCPD angles and the converter operating conditions.

Defining the THD of the CMV as [37]

$$\mathrm{THD}_{\mathrm{CMV}} = \frac{2}{V_{\mathrm{dc}}} \sqrt{\sum\nolimits_{m=1}^{3} \sum\nolimits_{n=-\infty}^{\infty} {Q_{mn}}^2}. \tag{18}$$

In this article, the working mode with the minimum THD$_{\mathrm{CMV}}$ value is referred to as the minimum CMV harmonics (Min-CMVH) mode.

By exhaustively evaluating the THD$_{\mathrm{CMV}}$ values for all P2PCPD angle pairs under different N and M, it is found that:

1) The P2PCPD angle corresponding to the minimum value of THD$_{\mathrm{CMV}}$ is not always (0, 0), but may also be $(\frac{2\pi}{3N}, \frac{4\pi}{3N})$ or $(\frac{4\pi}{3N}, \frac{2\pi}{3N})$ in some operating conditions.
2) The new P2PCPD angle pairs $(\frac{2\pi}{3N}, \frac{4\pi}{3N})$ and $(\frac{4\pi}{3N}, \frac{2\pi}{3N})$ share the same value of THD$_{\mathrm{CMV}}$.

Fig. 7 provides a quantitative comparison of the THD$_{\mathrm{CMV}}$ values under different cases. It is evident that the THD of the CMV can be further reduced by using the new P2PCPD angle pair under specific operating conditions, which is beneficial for CMV-sensitive systems. E.g., when $N = 5$ and $M = 0.95$, the THD value of the CMV can be reduced from 16.38% to 10.01% by using the new P2PCPD angle pairs.

Moreover, by comparing Figs. 4 and 7, it is clear that the horizontal coordinates of the intersection points marked in both figures are identical, and the THD performance between the CMV and the LLVs is complementary to each other. Consequently, the optimal P2PCPD angle pair selection criteria for the Min-CMVH mode can be directly obtained from Fig. 5. In contrast to the Min-LVH mode, (0, 0) should be chosen when the MMC operates in the white regions, whereas $(\frac{2\pi}{3N}, \frac{4\pi}{3N})$ or $(\frac{4\pi}{3N}, \frac{2\pi}{3N})$ should be selected when the MMC operates in the black regions. This makes sense since the CMV is common

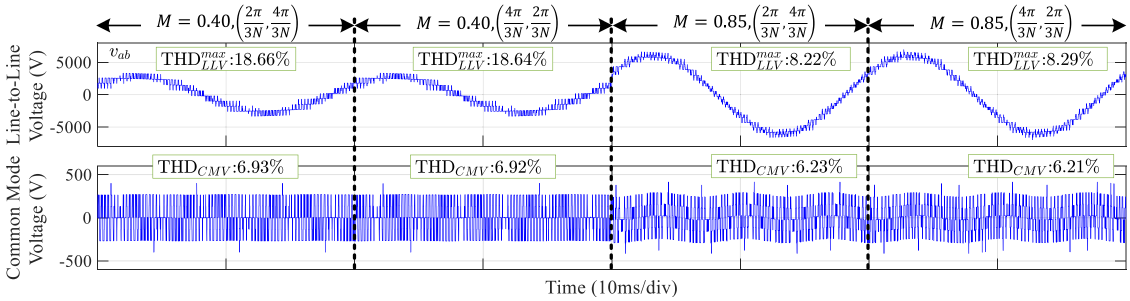

Fig. 17. Simulation waveforms of the Min-LVH mode across different modulation indexes at $N = 10$ and a power factor of 0.95 (Load 1).

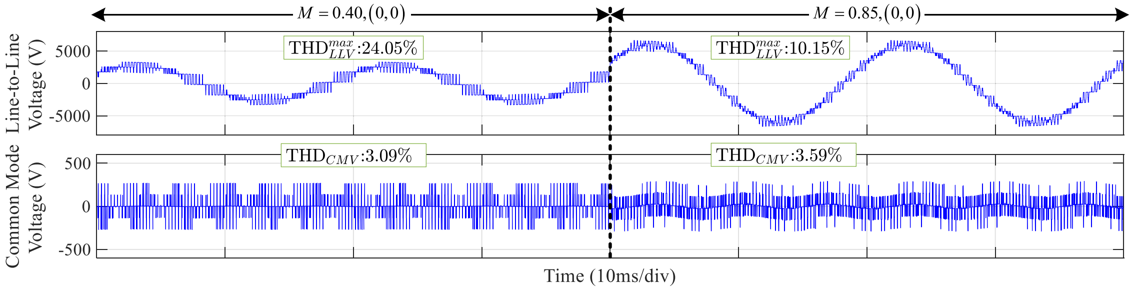

Fig. 18. Simulation waveforms of the Min-CMVH mode across different modulation indexes at $N = 10$ and a power factor of 0.95 (Load 1).

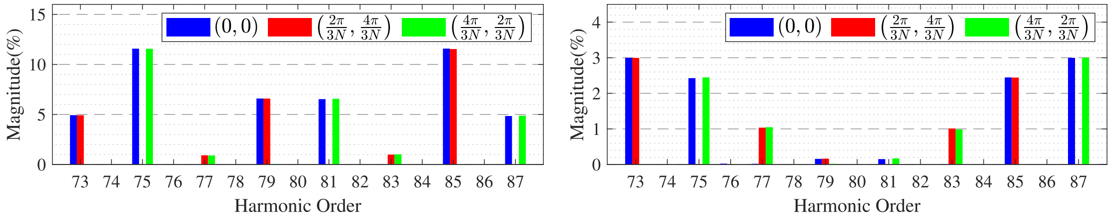

(a) (b)

Fig. 19. Simulation harmonic spectrum of the first carrier harmonic group of the LLVs across different modulation indexes at $N = 10$ and Load 1. (a) $M = 0.40$. (b) $M = 0.85$.

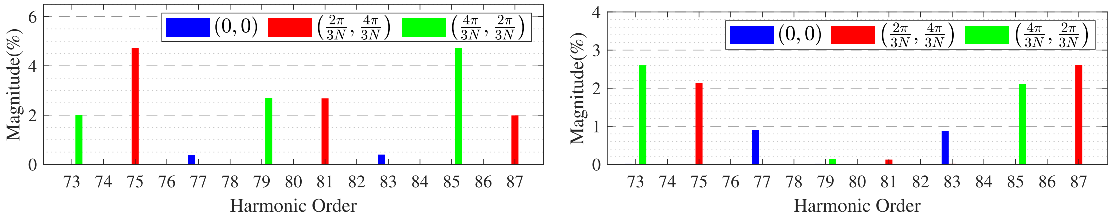

(a) (b)

Fig. 20. Simulation harmonic spectrum of the first carrier harmonic group of the CMV across different modulation indexes at $N = 10$ and Load 1. (a) $M = 0.40$. (b) $M = 0.85$.

TABLE IV
SIMULATION THD PERFORMANCE ACROSS DIFFERENT M AND (δ_1, δ_2) AT $N = 10$ AND LOAD 1

Item	$M = 0.40$			$M = 0.85$			
	$(0,0)$	$\left(\frac{2\pi}{3N},\frac{4\pi}{3N}\right)$	$\left(\frac{4\pi}{3N},\frac{2\pi}{3N}\right)$	$(0,0)$	$\left(\frac{2\pi}{3N},\frac{4\pi}{3N}\right)$	$\left(\frac{4\pi}{3N},\frac{2\pi}{3N}\right)$	$(0.13, 0.26)$
$\mathrm{THD}_{\mathrm{LLV}}^{\mathrm{max}}$ (%)	24.05	18.66	18.64	10.15	8.22	8.29	9.20
$\mathrm{THD}_{\mathrm{CMV}}$ (%)	3.09	6.93	6.92	3.59	6.23	6.21	5.66

TABLE V
SIMULATION THD PERFORMANCE ACROSS DIFFERENT P2PCPD ANGLE PAIRS AT $N = 10, M = 0.85$ AND LOAD 2

Item	$(0, 0)$	$(\frac{2\pi}{3N}, \frac{4\pi}{3N})$	$(\frac{4\pi}{3N}, \frac{2\pi}{3N})$	$(0.13, 0.26)$
$\mathrm{THD}_{\mathrm{LLV}}^{\max}$ (%)	9.14	7.18	7.22	8.17
$\mathrm{THD}_{\mathrm{CMV}}$ (%)	2.96	5.76	5.80	5.16

mode component of phase voltages and are cancelled out when the LLVs are formed.

In Fig. 8, the differences in CMV harmonic performance when using different P2PCPD angle pairs are compared across various values of N. The solid line denotes the P2PCPD angle pair $(0, 0)$, while the dotted line denotes the P2PCPD angle pair $(\frac{2\pi}{3N}, \frac{4\pi}{3N})$ or $(\frac{4\pi}{3N}, \frac{2\pi}{3N})$. As can be seen in Fig. 8, although the THD of CMV generally decreases with the increase of N, the relative differences in using different P2PCPD angle pairs are still clear. This indicates that the proposed selection criteria for the Min-CMVH mode remain effective when N is increased between 10 and 20. Therefore, the proposed selection criteria for the Min-CMVH mode are more suitable for the MV applications, similar to the Min-LVH mode.

IV. COMPREHENSIVE DESIGN OF THE P2PCPD ANGLES

When implementing the PSC–PWM scheme in MMC systems, the Min-LVH or the Min-CMVH mode can be achieved by directly selecting the corresponding P2PCPD angles based on Fig. 5. However, these two modes can not be achieved simultaneously. Fortunately, a trade-off mode between them can be developed by evaluating other nonzero P2PCPD angle pairs.

The blue region in Fig. 9 depicts all possible LLVs and CMV harmonic distortions when $M = 0.95$ and $N = 4$. Hence, the red boundary represents the optimal trade-off modes. For example, in order to determine the P2PCPD angle pairs corresponding to these trade-off modes, we can solve an optimization problem defined as follows:

$$\begin{aligned} &\min \ \mathrm{THD}_{\mathrm{CMV}}(\delta_1, \delta_2) \\ &\text{s.t.} \ \mathrm{THD}_{\mathrm{LLV}}^{\max} \leq D \\ &\qquad 0 \leq \delta_1 \leq \frac{2\pi}{N}, \quad 0 \leq \delta_2 \leq \frac{2\pi}{N} \end{aligned} \tag{19}$$

where D denotes the upper boundary of the maximum THD value of LLVs. Similarly, a proper set of P2PCPD angles can also be obtained by minimizing the $\mathrm{THD}_{\mathrm{LLV}}^{\max}$ value while keeping $\mathrm{THD}_{\mathrm{CMV}}$ value below a preset threshold D.

The threshold value D can also be determined by

$$\begin{aligned} D = &\min\left\{\mathrm{THD}_{\mathrm{LLV}}^{\max}(0,0), \mathrm{THD}_{\mathrm{LLV}}^{\max}\left(\tfrac{2\pi}{3N}, \tfrac{4\pi}{3N}\right)\right\} \\ &+ \lambda\left|\mathrm{THD}_{\mathrm{LLV}}^{\max}(0,0) - \mathrm{THD}_{\mathrm{LLV}}^{\max}\left(\tfrac{2\pi}{3N}, \tfrac{4\pi}{3N}\right)\right| \end{aligned} \tag{20}$$

where the weighting factor λ is between 0 and 1. A larger value of λ translates to enhanced CMV performance at the cost of LLV performance and vice versa.

The optimization problem (19) can be easily solved through an exhaustive search or other intelligent searching algorithms [38], [39]. The exhaustive search is more recommended since there are only two decision variables, and the corresponding search ranges are not large.

As an example, for the operating condition where $N = 4$ and $M = 0.95$, the calculated theoretical $\mathrm{THD}_{\mathrm{LLV}}^{\max}$ values that correspond to the Min-LVH and Min-CMVH modes are 21.5% and 26.0%, respectively. In this case, the threshold D is set to 25.0%. By solving (19) with a search step of 0.01, the P2PCPD angle pair is finally determined to be $(0.24, 0.48)$. Furthermore, it is worth noting that unlike the angle pairs $(0, 0)$, $(\frac{2\pi}{3N}, \frac{4\pi}{3N})$, and $(\frac{4\pi}{3N}, \frac{2\pi}{3N})$, the THD_y values under $(0.24, 0.48)$ are not equal, with $[\mathrm{THD}_{ab}, \mathrm{THD}_{bc}, \mathrm{THD}_{ca}] = [24.98\%, 24.98\%, 22.14\%]$.

Fig. 10 shows the overall flowchart of the implementation of the proposed method. For practical implementation of the trade-off mode, an offline 2-D look-up table (LUT), in terms of variables M and D, should be preconstructed. With this LUT, users can adjust the weighting factor λ or the threshold D online based on the actual grid code standards [40], [41] or users' specific requirements.

Fig. 11 illustrates the overall framework of the proposed PSC–PWM modulation for an MMC, where the selection criteria for (δ_1, δ_2) are stored in a LUT. Based on the LUT and the current operating conditions, the three-phase triangular carriers are appropriately phase-shifted. Subsequently, these phase-shifted carriers are compared with the modulation signals to generate the final gate pulses for each SM [19], [25].

V. SIMULATION RESULTS

In order to verify the correctness of the theoretical analysis in this article, a three-phase MMC model is built in MATLAB/Simulink software to simulate the effects of the P2PCPD angles on the harmonic performances under different operating conditions.

A. *Case 1: $N = 4$*

In Case 1, there are 4 SMs in one arm and the detailed simulation parameters of Case 1 are listed in Table I.

Figs. 12 and 13 show the simulation waveforms of the LLV and CMV under the Min-LVH and Min-CMVH mode, respectively. The corresponding THD values are summarized in Table II. When $M = 0.75$, the $\mathrm{THD}_{\mathrm{LLV}}^{\max}$ value under $(0, 0)$ is 28.78%, which is lower than that under $(\frac{2\pi}{3N}, \frac{4\pi}{3N})$ and $(\frac{4\pi}{3N}, \frac{2\pi}{3N})$; however, the $\mathrm{THD}_{\mathrm{CMV}}$ value under $(0, 0)$ is 20.73%, which is higher than that under $(\frac{2\pi}{3N}, \frac{4\pi}{3N})$ and $(\frac{4\pi}{3N}, \frac{2\pi}{3N})$. Consequently, $(0, 0)$ should be selected in the Min-LVH mode; while $(\frac{2\pi}{3N}, \frac{4\pi}{3N})$ or $(\frac{4\pi}{3N}, \frac{2\pi}{3N})$ should be selected in the Min-CMVH mode. When $M = 0.95$, the selection criteria for the P2PCPD angle pairs are inverted. These selection criteria are consistent with the summary in Fig. 5.

Fig. 14(a) and (b) shows the simulation harmonic spectrum of the first carrier harmonic group of the LLVs at $M = 0.75$ and $M = 0.95$, respectively. In comparison with the harmonic magnitude under $(0, 0)$, the 75_{th}, 81_{st}, and 87_{th} harmonics are well eliminated under $(\frac{2\pi}{3N}, \frac{4\pi}{3N})$; whereas the 73_{rd}, 79_{th}, and 85_{th} harmonics are well eliminated under $(\frac{4\pi}{3N}, \frac{2\pi}{3N})$. On the other hand, Fig. 15(a) and (b) shows the simulation harmonic spectrum of the first carrier harmonic group of the CMV at $M = 0.75$ and

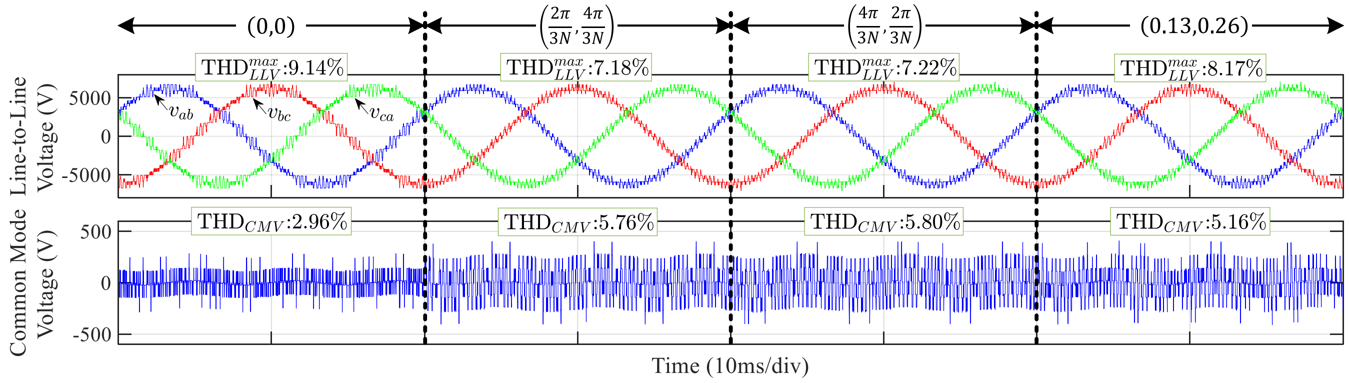

Fig. 21. Simulation waveforms across different P2PCPD angle pairs at $N = 10$, $M = 0.85$ and a power factor of 0.19 (Load 2).

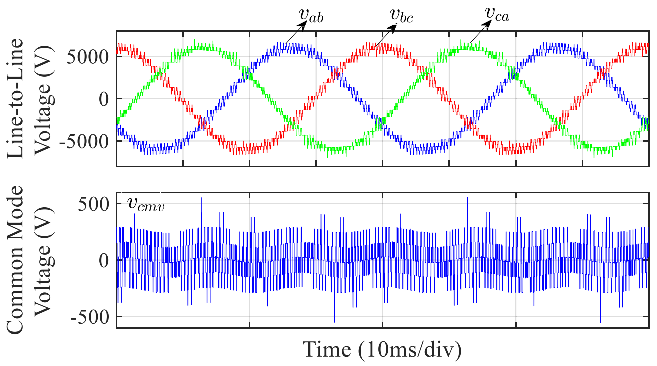

Fig. 22. Simulation waveforms of the LLVs and the CMV with Load 1 when $N = 10$, $M = 0.85$ and $(\delta_1, \delta_2) = (0.13, 0.26)$.

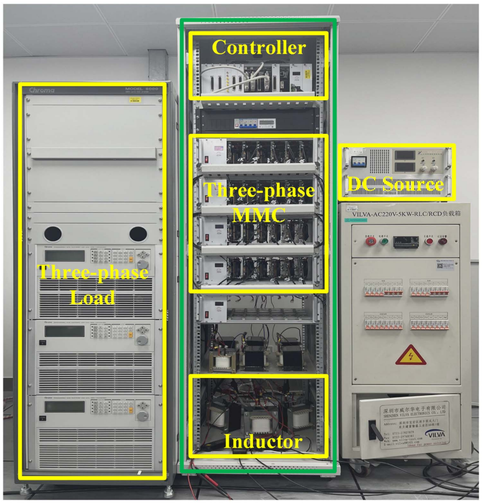

Fig. 23. Experimental platform.

$M = 0.95$, respectively. Compared with the magnitude of the CMV harmonics under (0, 0), the $77_{\rm th}$ and $83_{\rm rd}$ CMV harmonics are well eliminated under $(\frac{2\pi}{3N}, \frac{4\pi}{3N})$ and $(\frac{4\pi}{3N}, \frac{2\pi}{3N})$. By further comparing Fig. 15(a) and (b), it is evident that the relative amplitude of the remaining side-band harmonics under different P2PCPD angle pairs varies with the modulation index, which intuitively explains why the optimal P2PCPD angle pair changes with the modulation index.

Fig. 16 displays the simulation waveforms when $M = 0.95$ and $(\delta_1, \delta_2) = (0.24, 0.48)$, which is the angle pair obtained in Section IV for the trade-off between LLV and CMV harmonics. The corresponding simulation $\text{THD}_{\text{LLV}}^{\text{max}}$ and THD_{CMV} values are 25.99% and 15.09%, respectively. Table II summarizes the harmonic performance of different cases. Combing with Table II, it is clear that a trade-off performance is achieved by using the proposed design method.

B. Case 2: $N = 10$

In Case 2, there are 10 SMs in one arm and the detailed simulation parameters of Case 2 are listed in Table III.

Figs. 17 and 18 show the simulation waveforms with Load 1 under the Min-LVH and Min-CMVH mode, respectively. The corresponding THD values are summarized in Table IV. When $M = 0.85$, compared to (0, 0), the P2PCPD angle pair $(\frac{2\pi}{3N}, \frac{4\pi}{3N})$ and $(\frac{4\pi}{3N}, \frac{2\pi}{3N})$ suggested by the Min-LVH mode can reduce the value $\text{THD}_{\text{LLV}}^{\text{max}}$ from 10.15% to 8.22% and 8.29%, respectively, which denotes approximately a reduction of 18% in the LLV harmonics. However, the P2PCPD angle pair $(\frac{2\pi}{3N}, \frac{4\pi}{3N})$ and $(\frac{4\pi}{3N}, \frac{2\pi}{3N})$ worsens the CMV performance. Compared with the P2PCPD angle pair (0, 0) suggested by Min-CMVH mode, the value of THD_{CMV} increases from 3.59% to 6.23% and 6.21%. When $M = 0.40$, the proposed P2PCPD angle selection criteria in Fig. 5 are also correct.

Fig. 19 shows the simulation harmonic spectrum of the LLVs at different modulation indexes with Load 1. Fig. 20 shows the harmonic spectrum of the CMV. As can be seen from Figs. 19 and 20, the P2PCPD angle pair suggested by the proposed angle selection criteria always corresponds to lower amplitude of the remaining side-band harmonics.

By setting the threshold D to 9.5%, corresponding to $\lambda = 0.58$, the trade-off P2PCPD angle pair is determined to be (0.13,0.26) when $M = 0.85$. Fig. 22 displays the simulation waveforms of the LLVs and CMV with Load 1 when $M = 0.85$ and $(\delta_1, \delta_2) = (0.13, 0.26)$. The corresponding simulation $\text{THD}_{\text{LLV}}^{\text{max}}$ and THD_{CMV} values are 9.20% and 5.66%,

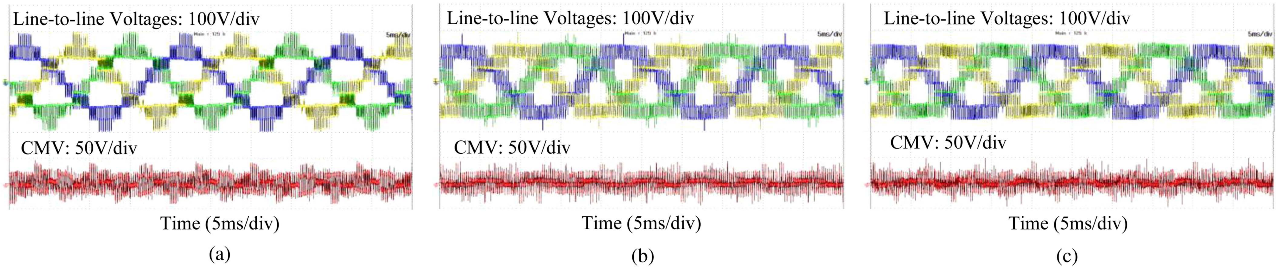

Fig. 24. Experimental waveforms at $M = 0.75$. (a) $(\delta_1, \delta_2) = (0, 0)$. (b) $(\delta_1, \delta_2) = (\frac{2\pi}{3N}, \frac{4\pi}{3N})$. (c) $(\delta_1, \delta_2) = (\frac{4\pi}{3N}, \frac{2\pi}{3N})$.

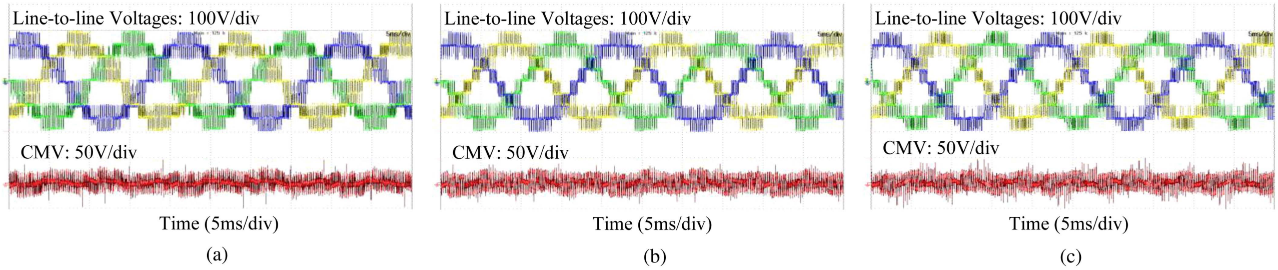

Fig. 25. Experimental waveforms at $M = 0.95$. (a) $(\delta_1, \delta_2) = (0, 0)$. (b) $(\delta_1, \delta_2) = (\frac{2\pi}{3N}, \frac{4\pi}{3N})$. (c) $(\delta_1, \delta_2) = (\frac{4\pi}{3N}, \frac{2\pi}{3N})$.

TABLE VI
EXPERIMENTAL THD PERFORMANCE UNDER DIFFERENT M AND (δ_1, δ_2)

Item	$M = 0.75$			$M = 0.95$			
	$(0, 0)$	$(\frac{2\pi}{3N}, \frac{4\pi}{3N})$	$(\frac{4\pi}{3N}, \frac{2\pi}{3N})$	$(0, 0)$	$(\frac{2\pi}{3N}, \frac{4\pi}{3N})$	$(\frac{4\pi}{3N}, \frac{2\pi}{3N})$	$(0.24, 0.48)$
$\text{THD}_{\text{LLV}}^{\max}$ (%)	30.84	35.63	36.22	27.86	24.52	24.32	26.64
THD_{CMV} (%)	21.14	16.70	16.73	14.10	17.73	18.39	16.67

respectively. Table IV summarizes the harmonic performance of different cases. Combined with Table IV, it is clear that a trade-off performance is achieved by using the proposed design method.

Fig. 21 shows the simulation waveforms of the LLVs and CMV at a low power factor of 0.19 (Load 2). The corresponding THD values are summarized in Table V. It can be seen that (0, 0) suggested by the Min-CMVH mode corresponds to better harmonic performance at CMV, while $(\frac{2\pi}{3N}, \frac{4\pi}{3N})$ and $(\frac{4\pi}{3N}, \frac{2\pi}{3N})$ suggested by the Min-LVH mode correspond to better harmonic performance at LLVs. Furthermore, it is also clear that a trade-off performance is achieved with the derived trade-off angle. Therefore, the proposed design method for the P2PCPD angles also holds at low power factors.

VI. EXPERIMENT RESULTS

In order to verify the correctness of the theoretical analysis in this article, experiments are carried out on a three-phase MMC prototype, as shown in Fig. 23. The PSC-PWM modulation scheme is implemented on an RTU-BOX204 controller, and the corresponding experimental parameters are listed in Table I.

Figs. 24 and 25 show the experimental waveforms of the LLVs, CMV at $M = 0.75$ and $M = 0.95$, respectively. The corresponding experimental THD values are summarized in Table VI. When $M = 0.75$, the $\text{THD}_{\text{LLV}}^{\max}$ value under (0, 0) is 30.84%, which is lower than that under $(\frac{2\pi}{3N}, \frac{4\pi}{3N})$ and $(\frac{4\pi}{3N}, \frac{2\pi}{3N})$; however, the THD_{CMV} value under (0, 0) is 21.14%, which is higher than that under $(\frac{2\pi}{3N}, \frac{4\pi}{3N})$ and $(\frac{4\pi}{3N}, \frac{2\pi}{3N})$. Consequently, (0, 0) should be selected in the Min-LVH mode; while $(\frac{2\pi}{3N}, \frac{4\pi}{3N})$ or $(\frac{4\pi}{3N}, \frac{2\pi}{3N})$ should be selected in the Min-CMVH mode. When $M = 0.95$, the selection criteria of the P2PCPD angle pairs are inverted. These selection criteria again verify the summary in Fig. 5.

Fig. 26 shows the experimental harmonic spectrum of the LLVs at different modulation indexes. Fig. 27 shows the harmonic spectrum of the CMV. The recorded harmonic suppression characteristics are consistent with the simulation results.

Fig. 28 shows the experimental waveforms when $M = 0.95$ and $(\delta_1, \delta_2) = (0.24, 0.48)$. The corresponding $\text{THD}_{\text{LLV}}^{\max}$ and THD_{CMV} values are 26.64% and 16.67%, respectively. Table VI summarizes the experimental harmonic performance of different cases. Combing with Table VI, it is clear that a trade-off performance can be achieved by using the proposed comprehensive design method.

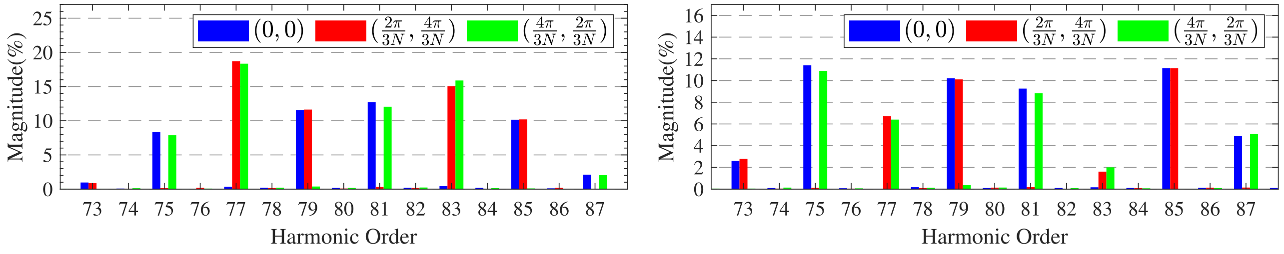

(a) (b)

Fig. 26. Experimental harmonic spectrum of the first carrier harmonic group of the LLVs at different modulation indexes. (a) $M = 0.75$. (b) $M = 0.95$.

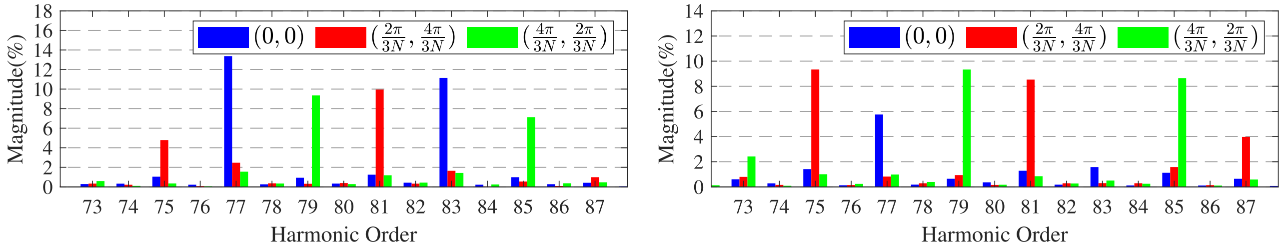

(a) (b)

Fig. 27. Experimental harmonic spectrum of the first carrier harmonic group of the CMV at different modulation indexes. (a) $M = 0.75$. (b) $M = 0.95$.

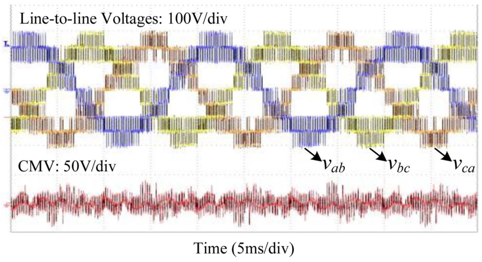

Fig. 28. Experimental waveforms of the LLVs and the CMV when $M = 0.95$ and $(\delta_1, \delta_2) = (0.24, 0.48)$.

VII. CONCLUSION

This article presents an analysis of the P2PCPD angles in the MMC systems with PSC–PWM. The Double-Fourier method is employed to quantify the harmonic features of the LLVs and CMV. It is found that the harmonic magnitudes of both LLVs and CMV are functions of P2PCPD angles. Based on this analysis, the Min-LVH mode and Min-CMVH mode are developed, catering to different application scenarios. The corresponding selection criteria are proposed for different conditions in terms of the modulation index and the numbers of SMs per arm of the MMC. Moreover, it is revealed that the Min-LVH and Min-CMVH modes cannot be achieved at the same time. For a flexible trade-off between both modes, a straightforward optimization problem can be formulated to select proper P2PCPD angles. However, since the implementation effort and the switching losses of the PSC-PWM scheme significantly increase with the number of SMs, the proposed analysis and design method are not suitable for applications with a large number of SMs, such as high voltage applications. Nevertheless, it is beneficial to consider the proposed analysis and design method for MV applications with a relatively low number of SMs, such as MV motor drive and MMC-based MVDC distribution grid applications, where effective suppression of LLV or CMV harmonics can be achieved without increasing the hardware cost.

From the conducted simulations and experiments, it can be concluded: 1) the P2PCPD angle pair suggested by the proposed angle selection criteria for the Min-LVH (Min-CMVH) mode always corresponds to lower THD values of LLVs (CMV). 2) The derived trade-off P2PCPD angles achieve a trade-off performance between the LLVs and CMV. Conclusively, simulations and experiments validate the theoretical findings.

REFERENCES

[1] M. Guan and Z. Xu, "Modeling and control of a modular multilevel converter-based HVDC system under unbalanced grid conditions," *IEEE Trans. Power Electron.*, vol. 27, no. 12, pp. 4858–4867, Dec. 2012.

[2] F. Zhao, G. Xiao, T. Zhu, X. Zheng, Z. Wu, and T. Zhao, "A coordinated strategy of low-speed and start-up operation for medium-voltage variable-speed drives with a modular multilevel converter," *IEEE Trans. Power Electron.*, vol. 35, no. 1, pp. 709–724, Jan. 2020.

[3] J. Lyu, X. Cai, and M. Molinas, "Frequency domain stability analysis of MMC-based HVdc for wind farm integration," *IEEE J. Emerg. Sel. Topics Power Electron.*, vol. 4, no. 1, pp. 141–151, Mar. 2016.

[4] S. Debnath, J. Qin, B. Bahrani, M. Saeedifard, and P. Barbosa, "Operation, control, and applications of the modular multilevel converter: A review," *IEEE Trans. Power Electron.*, vol. 30, no. 1, pp. 37–53, Jan. 2015.

[5] A. Dekka, B. Wu, R. L. Fuentes, M. Perez, and N. R. Zargari, "Evolution of topologies, modeling, control schemes, and applications of modular multilevel converters," *IEEE J. Emerg. Sel. Topics Power Electron.*, vol. 5, no. 4, pp. 1631–1656, Dec. 2017.

[6] Y. Zhu, S. Jiang, J. Pou, and G. Konstantinou, "Virtual arm impedance emulation and stability improvement in modular multilevel converters," *IEEE Trans. Power Electron.*, vol. 39, no. 4, pp. 3931–3942, Apr. 2024.

[7] P. Hu and D. Jiang, “A level-increased nearest level modulation method for modular multilevel converters,” *IEEE Trans. Power Electron.*, vol. 30, no. 4, pp. 1836–1842, Apr. 2015.

[8] Q. Xiao et al., “Decoupled control scheme for THD reduction and one specific harmonic elimination in the modular multilevel converter,” *IEEE Trans. Ind. Electron.*, vol. 70, no. 1, pp. 99–111, Jan. 2023.

[9] W. Wang, K. Ma, and X. Cai, “Flexible nearest level modulation for modular multilevel converter,” *IEEE Trans. Power Electron.*, vol. 36, no. 12, pp. 13686–13696, Dec. 2021.

[10] G. P. Adam, O. Anaya-Lara, G. M. Burt, D. Telford, B. W. Williams, and J. R. McDonald, “Modular multilevel inverter: Pulse width modulation and capacitor balancing technique,” *IET Power Electron.*, vol. 3, no. 5, pp. 702–715, Sep. 2010.

[11] M. Saeedifard and R. Iravani, “Dynamic performance of a modular multilevel back-to-back HVDC system,” *IEEE Trans. Power Del.*, vol. 25, no. 4, pp. 2903–2912, Oct. 2010.

[12] J. Mei, K. Shen, B. Xiao, L. M. Tolbert, and J. Zheng, “A new selective loop bias mapping phase disposition PWM with dynamic voltage balance capability for modular multilevel converter,” *IEEE Trans. Ind. Electron.*, vol. 61, no. 2, pp. 798–807, Feb. 2014.

[13] R. Darus, J. Pou, G. Konstantinou, S. Ceballos, R. Picas, and V. G. Agelidis, “A modified voltage balancing algorithm for the modular multilevel converter: Evaluation for staircase and phase-disposition PWM,” *IEEE Trans. Ind. Electron.*, vol. 30, no. 8, pp. 4119–4127, Aug. 2015.

[14] F. Deng, Q. Yu, Q. Wang, R. Zhu, X. Cai, and Z. Chen, “Suppression of dc-Link current ripple for modular multilevel converters under phase-disposition PWM,” *IEEE Trans. Power Electron.*, vol. 35, no. 3, pp. 3310–3324, Mar. 2020.

[15] S. Kouro et al., “Recent advances and industrial applications of multilevel converters,” *IEEE Trans. Ind. Electron.*, vol. 57, no. 8, pp. 2553–2580, Aug. 2010.

[16] Y. Zhang, J. Zhang, and F. Deng, “Improved CPS-PWM approach for over-modulation operations of hybrid modular multilevel converter,” *IEEE J. Emerg. Sel. Topics Power Electron.*, vol. 10, no. 5, pp. 5933–5943, Oct. 2022.

[17] R. Naderi and A. Rahmati, “Phase-shifted carrier PWM technique for general cascaded inverters,” *IEEE Trans. Power Electron.*, vol. 23, no. 3, pp. 1257–1269, May 2008.

[18] K. Ilves, L. Harnefors, S. Norrga, and H.-P. Nee, “Analysis and operation of modular multilevel converters with phase-shifted carrier PWM,” *IEEE Trans. Power Electron.*, vol. 30, no. 1, pp. 268–283, Jan. 2015.

[19] B. Li, R. Yang, D. Xu, G. Wang, W. Wang, and D. Xu, “Analysis of the phase-shifted carrier modulation for modular multilevel converters,” *IEEE Trans. Power Electron.*, vol. 30, no. 1, pp. 297–310, Jan. 2015.

[20] S. Lu, L. Yuan, K. Li, and Z. Zhao, “An improved phase-shifted carrier modulation scheme for a hybrid modular multilevel converter,” *IEEE Trans. Power Electron.*, vol. 32, no. 1, pp. 81–97, Jan. 2017.

[21] C. Xu, L. Lin, T. Yin, and J. Hu, “An improved phase-shifted-carrier technique for hybrid modular multilevel converter with boosted modulation index,” *IEEE Trans. Power Electron.*, vol. 35, no. 2, pp. 1340–1352, Feb. 2020.

[22] H. Jiang, F. Deng, Z. Wang, Z. Zou, B. Li, and F. Blaabjerg, “Harmonic optimization strategy for CPS-PWM based MMCs under submodule capacitor voltage reduction control,” *IEEE Trans. Power Electron.*, vol. 37, no. 4, pp. 4288–4300, Apr. 2022.

[23] S. S. Thakur, M. Odavic, A. Allu, Z. Q. Zhu, and K. Atallah, “Analytical modelling and optimization of output voltage harmonic spectra of full-bridge modular multilevel converters in boost mode,” *IEEE Trans. Power Electron.*, vol. 37, no. 3, pp. 3403–3420, Mar. 2022.

[24] B. Li, L. Han, S. Mao, S. Zhou, Z. Qu, and D. Xu, “Decoupled modulation scheme for modular multilevel converters in medium-voltage applications,” *IEEE Trans. Power Electron.*, vol. 35, no. 11, pp. 11430–11441, Nov. 2020.

[25] Z. Zhou, N. Dai, L. Liu, and J. Yin, “Dual-phase-shifted pulse width modulation of three-phase modular multilevel converters,” *IEEE Trans. Ind. Electron.*, vol. 71, no. 2, pp. 1927–1937, Feb. 2024.

[26] D. G. Holmes and T. A. Lipo, *Pulse Width Modulation of Power Converters: Principles and Practice*. Hoboken, NJ, USA: Wiley, 2003.

[27] S. B. Bashir et al., “Modular multilevel converter-based microgrid: A critical review,” *IEEE Access*, vol. 11, pp. 65569–65589, 2023.

[28] Siemens, “Medium voltage drives SINAMICS perfect harmony GH150,” Accessed: Mar. 13, 2024. [Online]. Available: https://assets.new.siemens.com/siemens/assets/api/uuid:18aa6fa6-7bfa-450a-8328-2cfe787e8844/gh150acbrochurejune2019.pdf

[29] L. Lin, Y. Lin, Z. He, Y. Chen, J. Hu, and W. Li, “Improved nearest-level modulation for a modular multilevel converter with a lower submodule number,” *IEEE Trans. Power Electron.*, vol. 31, no. 8, pp. 5369–5377, Aug. 2016.

[30] T. Plazenet, T. Boileau, C. Caironi, and B. Nahid-Mobarakeh, “A comprehensive study on shaft voltages and bearing currents in rotating machines,” *IEEE Trans. Ind. Appl.*, vol. 54, no. 4, pp. 3749–3759, Jul./Aug. 2018.

[31] Y. Han, H. Lu, Y. Li, and J. Chai, “Analysis and suppression of shaft voltage in SiC-based inverter for electric vehicle applications,” *IEEE Trans. Power Electron.*, vol. 34, no. 7, pp. 6276–6285, Jul. 2019.

[32] F. Acosta-Cambranis, J. Zaragoza, N. Berbel, G. J. Capella, and L Romeral, “Constant common-mode voltage strategies using sigma–delta modulators in five-phase VSI,” *IEEE Trans. Ind. Electron.*, vol. 70, no. 3, pp. 2189–2198, Mar. 2023.

[33] M. Wu et al., “A discrete selective harmonic elimination formulation with common-mode voltage elimination ability,” *IEEE Trans. Power Electron.*, vol. 39, no. 4, pp. 3962–3967, Apr. 2024.

[34] G. Eugenio, P. Sanchis, A. Ursua, J. Lopez, and L. Marroyo, “Ground currents in single-phase transformerless photovoltaic systems,” *Photovolt., Res. Appl.*, vol. 15, no. 7, pp. 629–650, 2007.

[35] M. S. Hassan, A. Abdelhakim, M. Shoyama, J. Imaoka, and G. M. Dousoky, “Parallel operation of split-source inverters for PV systems: Analysis and modulation for circulating current and EMI noise reduction,” *IEEE Trans. Power Electron.*, vol. 36, no. 8, pp. 9547–9564, Aug. 2021.

[36] P. Zhao, X. He, Y. Wang, C. Qiu, and P. Han, “Hardware-based modulation strategy to suppress the leakage current for transformerless odd-module cascaded H-bridge inverter in PV system,” *IEEE Trans. Power Electron.*, vol. 39, no. 3, pp. 3655–3667, Mar. 2024.

[37] A. M. Alcaide et al., “Generalized multicarrier PWM technique for two-level voltage source inverters,” *IEEE Trans. Ind. Electron.*, vol. 70, no. 5, pp. 4345–4355, May 2023.

[38] J. Kennedy and R. Eberhart, “Particle swarm optimization,” in *Proc. Int. Conf. Neural Netw.*, Perth, WA, Australia, 1995, pp. 1942–1948.

[39] S. S. Rao, *Engineering Optimization.*, Hoboken, NJ, USA: Wiley, 2009.

[40] *Harmonic Voltage Distortion and the Connection of Harmonic Sources and/or Resonant Plant to Transmission Systems and Distribution Networks in the United Kingdom*, ENA EREC G5 Issue 5, Jun. 2020. Accessed: Mar. 13, 2024. [Online]. Available: https://www.dcode.org.uk/assets/uploads/ENA_EREC_G5_Issue_5__2020_.pdf

[41] *IEEE Recommended Practice and Requirements for Harmonic Control in Electric Power Systems*, IEEE Standard 519-2014 (Revision of IEEE Standard 519-1992), Jun. 2014, pp. 1–29, doi: 10.1109/IEEESTD.2014.6826459.

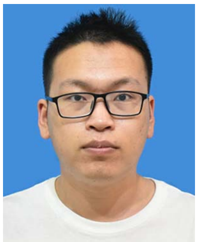

Bin Zhang (Student Member, IEEE) was born in Inner Mongolia, China. He received the B.S. degree in electrical engineering and its automation from the University of Electronic Science and Technology of China, Chengdu, China, in 2021. He is currently working toward the Ph.D. degree in electrical and computer engineering, University of Macau, Macau, China.

His research interests include the control and modulation strategies of modular multilevel converters.

Jiapeng Yin was born in Shenyang, China. He received the B.S. degree in automation and the M.S. degree in control science and engineering from the Harbin Institute of Technology, Harbin, China, in 2014 and 2016, respectively, and the Ph.D. degree in telecommunications engineering from the Universidad de Sevilla, Seville, Spain, in 2021.

He is currently a Postdoctoral Research Fellow with the University of Macau. His research interests include modulation and control of multilevel converters for high-power applications.

Qifan Yang received the B.Sc. degree in smart grid information engineering from the University of Electronic Science and Technology of China, Chengdu, China, in 2020. He is currently working toward the Ph.D. degree in electrical and computer engineering with the University of Macau, Macau, China.

His research interests include parameter design of power converters, application of artificial intelligence algorithms in power electronics, and data-driven digital twin modeling of power equipment.

Ningyi Dai (Senior Member, IEEE) received the B.Sc. degree in electrical engineering from Southeast University, Nanjing, China, in 2001, and the M.Sc. and Ph.D. degrees in electrical and electronics engineering from University of Macau, Macau, China, in 2004 and 2007, respectively.

She is currently an Associate Professor with the Department of Electrical and Computer Engineering and SKL of Internet of Things for Smart City, University of Macau. She is also the Assistant Dean of Faculty of Science and Technology, University of Macau. She has authored or coauthored more than 90 technical journals and conference papers in power systems and power electronics. Her research interests include the application of power electronics in power systems, control of power converters and integrated energy system.

Dr. Dai was the corecipient of the Macao Science and Technology Award in 2012, 2018, and 2022.